Cross-spectral matrix fitting for passive mapping of the ultrasonic cavitation based on Elastic-net regularization

Célestine Lachambre, Adrian Basarab, Jean-Christophe Bera, Barbara Nicolas, François Varray, Bruno Gilles

Cross-spectral matrix fitting for passive mapping of the ultrasonic cavitation based on Elastic-net regularization

Célestine Lachambre*†, Adrian Basarab*, Jean-Christophe Bera†, Barbara Nicolas*,
François Varray*, Bruno Gilles †

Email: celestine.lachambre@creatis.insa-lyon.fr
* CREATIS, Univ. Lyon, INSA-Lyon, Université Claude Bernard Lyon 1, UJM-Saint-Etienne, CNRS, Inserm, CREATIS UMR 5220, U1206, Lyon, France
†Université Lyon, Inserm U1032, LabTau, Université Claude Bernard Lyon 1, Lyon, France

***Abstract*—Cavitation produced by high-intensity focused ultrasound needs to be monitored for specific applications such as sonoporation. Passive acoustic mapping using adaptive or non-adaptive beamforming methods has been proposed in the literature for this task, but lacks of spatial (primarily axial) resolution. This is mainly due to the absence of a time reference, a common specificity of passive imaging compared to standard pulse-echo ultrasound. In this paper, we propose an inverse problem-based method for passive cavitation imaging, aiming to increase the spatial resolution through sparsity constraints. Results on simulated data are presented and compared to state-of-the-art approaches, such as the frequential delay-and-sum and the frequential robust Capon beamformer.**

***Index Terms*—Passive ultrasound imaging, beamforming, inverse problems, sparsity, cavitation imaging**

I. Introduction

High intensity focused ultrasound (HIFU) waves are used for a wide range of therapeutic applications, exploiting different effects such as heat, shock waves or cavitation [1]. For the latter, the pressure variations of the focused ultrasound waves cause bubble gas oscillation and implosion, creating either a harmonic or broadband response.

For safety and performance reasons, cavitation shall be localized during such treatments to monitor its effects and possibly to provide closed-loop control. Due to interference with the HIFU signals, active ultrasound imaging using ultrasound wave transmissions is not applicable. Gyöngy *et al.* [2] first introduced passive temporal acoustic mapping of the cavitation, that is more precisely a passive delay-and-sum (DAS) beamforming algorithm. Despite its interest, DAS fails in accurately localizing the cavitation, mainly because of its low axial resolution, intrinsically related to the lack of time reference. To overcome this major limitation, adaptive beamforming methods, such as robust Capon beamformer (RCB) [3], [4] have been adapted to passive imaging of the cavitation in [5]. Furthermore, the interest of frequency-based adaptive beamformers in cavitation imaging has been evaluated [6]. Both temporal and frequential adaptive beamformers improved the spatial resolution of DAS, at the cost of higher computational time, especially for temporal methods. Despite these improvements, classical beamformers initially proposed for active imaging and adapted to passive imaging, fail in achieving an axial spatial resolution equivalent to the lateral one, required for clinical applications.

Passive beamformers have been extensively studied in number of applications, such as for example in aeroacoustics [7]. One class of methods, that expresses the beamforming as the inversion of a direct model relating the raw radio-frequency (RF) data to the map of interest, is particularly interesting due to its ability of considering prior information about the imaged medium [7]. To the best of our knowledge, such methods have not been yet adapted nor evaluated in the cavitation imaging context. This represents the main objective of this work, with a particular focus on a cross spectral matrix fitting [8] and an elastic net regularization promoting the sparsity of the cavitation maps [9].

The remainder of the paper is organized as follows. We first present the developed method, then compare it with the state-of-the-art DAS and RCB on different simulations and conclude with a discussion.

II. Proposed method

This section presents the model used in this work, as well as the inversion method that permits to estimate a cavitation map from the raw RF data exploiting its spatial sparsity. Let us consider the case of an N-element linear array, that operates in passive mode and records N RF signals of T samples originating from a medium exposed to HIFU waves. We denote by $\mathbf{Y} \in \mathbb{R}^{N \times T}$ the matrix containing all the N RF signals, and by $\bar{\mathbf{Y}} \in \mathbb{C}^{N \times F}$ its corresponding version in the frequency domain, *i.e.*, in which each RF signal is replaced by its discrete Fourier transform containing F frequencies. In the following, we focus on one frequency, and thus consider as acquired data a vector $\bar{\mathbf{y}} \in \mathbb{C}^{N \times 1}$, that gathers the frequency samples corresponding to the same frequency for each of the N RF signals.

A. Cross-spectral matrix

From $\bar{\mathbf{y}}$, one can estimate the cross-spectral matrix (CSM) at a given frequency, denoted by $\mathbf{C} \in \mathbb{C}^{N \times N}$ and defined by:

$$\mathbf{C} = \mathbb{E}[\bar{\mathbf{y}}\bar{\mathbf{y}}^H], \tag{1}$$

where $\cdot^H$ stands for the complex conjugate and $\mathbb{E}[\cdot]$ is the expected value. Note that the CSM is also the central point of cavitation imaging beamformers working in the frequency domain. In practice, to improve the robustness of the CSM estimate, the temporal RF signals are divided in K overlapping time windows of length T_{snap} assimilated to different snapshots [4]:

$$\hat{\mathbf{C}} = \frac{1}{K}\sum_{k=1}^{K} \bar{\mathbf{y}}_k \bar{\mathbf{y}}_k^H, \tag{2}$$

where $\hat{\mathbf{C}}$ is a robust estimation of $\mathbf{C}$ and $\bar{\mathbf{y}}_k$ is the frequency vector corresponding to the k-th snaphot.

B. CSM-based forward model

Let us denote by $\mathbf{s} \in \mathbb{R}^{M \times 1}$ a discrete vectorized version of the cavitation map to be beamformed, where M is the total number of potential source positions on a rectangular grid. The signals received from one source at a given location impinging on N elements are related to that source by the corresponding steering vector. In the Fourier domain and considering the M potential source positions, a forward model can be established relating the frequency vector $\bar{\mathbf{y}}$ to the source map $\mathbf{s}$ using the model of spherical wave propagation described in [8]:

$$\bar{\mathbf{y}} = \mathbf{H}\mathbf{s}, \tag{3}$$

where $\mathbf{H} \in \mathbb{C}^{N \times M}$ is a matrix whose columns represent the steering vectors relating one source position to all elements. Injecting (3) in the model (1) gives:

$$\mathbf{C} = \mathbf{H}\mathbb{E}[\mathbf{s}\mathbf{s}^H]\mathbf{H}^H. \tag{4}$$

Note that $\mathbb{E}[\mathbf{s}\mathbf{s}^H]$ represents the cross-correlation matrix between the source grid positions. Assuming that cavitation sources are independent of each other, $\mathbb{E}[\mathbf{s}\mathbf{s}^H]$ becomes a diagonal matrix, where the main diagonal, denoted by $\mathbf{x} \in \mathbb{R}^{M \times 1}$, holds the power of each potential source on the beamforming grid.

Using basic algebra rules, the model in (4) can be rewritten as:

$$\hat{\mathbf{c}} = \mathbf{A}\mathbf{x} + \mathbf{n}, \tag{5}$$

where $\hat{\mathbf{c}} \in \mathbb{C}^{N^2 \times 1}$ is the vectorized version of the robust CSM, $\mathbf{A} \in \mathbb{C}^{N^2 \times M}$ is a reshaped steering matrix, $\mathbf{n} \in \mathbb{C}^{N^2 \times 1}$ is an additive white Gaussian noise accounting for measurement noise and model imperfections, and $\mathbf{x} \in \mathbb{R}^{M \times 1}$ is the vectorized form of the power map to be estimated.

C. Elastic net-based inversion

Inverting the model in (5), *i.e.*, estimating the power map $\mathbf{x}$ from the CSM robustly estimated from the acquired raw RF data, can be treated as a typical inverse problem. One common way to solve such an inverse problem is to express it as the minimization of a cost function, composed of a data fidelity term and a regularizer. In our case, based on the assumption that cavitation maps are sparse (only a few cavitation clouds can occur at the same time), the regularizer is a classical elastic net penalty [9], as follows:

$$\min_{\mathbf{x}} \frac{1}{2}\|\hat{\mathbf{c}} - \mathbf{A}\mathbf{x}\|_2^2 + \lambda_1\|\mathbf{x}\|_1 + \frac{\lambda_2}{2}\|\mathbf{x}\|_2^2, \tag{6}$$

where the first term is a quadratic data fidelity term resulting from the assumption of additive Gaussian noise, the second is an ℓ_1-norm promoting sparsity of the cavitation map, and the third one is an ℓ_2-norm ridge penalization, that slightly relaxes the sparsity constraint, thus allowing smooth cavitation spots. The two latter terms are respectively weighted by λ_1 and λ_2. We used a FISTA algorithm based on [10] for minimization.

III. Results

A. Simulation setup

To validate the proposed beamforming method, three simulations have been done, as described hereafter:

- a unique inertial cavitation source, representing a bubble placed at $(-5,\ 70)$ mm;
- two inertial cavitation sources laterally distributed at $(-0.7{,}70)$ and $(0.7{,}70)$ mm;
- two inertial cavitation sources axially distributed at $(0{,}65)$ and $(0{,}75)$ mm.

For all configurations, the cavitation signal was simulated as a broadband noise [11]. The linear probe simulated to generate the received RF signals had $N = 128$ elements, a central frequency of 5.5 MHz, a bandwidth at -6 dB spanning from 3.5 to 7.5 Mhz and a pitch of 300 µm.

The proposed method, referred to as CMF-Elastic-net, was compared to DAS from [6], [12] and frequency RCB [5], [6]. The hyperparameters were fixed, for each method, to their best values and kept constant over the three simulation configurations. In particular, the parameter used to condition the inversion of the CSM with RCB was fixed at 10, and $\lambda_1 = 90$ and $\lambda_2 = 10$ for CMF-Elastic-net.

The imaging was done at 3 MHz for all the methods and for all the configurations.

For all configurations, the three methods are compared through a power map, the profile of the lateral and axial lobe of those maps, as well as the size of the lobes at -3dB. Average position and standard deviations of the maximum of the sources were calculated from 100 different simulations.

B. One bubble

Figure 1 shows the reconstruction of one inertial bubble in highly noisy conditions (SNR of -5 dB) obtained with the three beamforming algorithms.

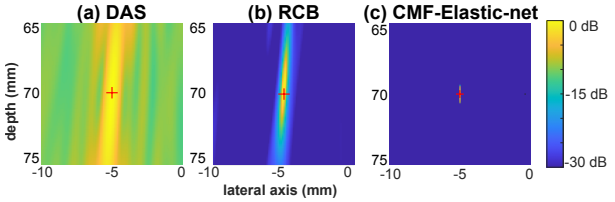

Fig. 1. Power maps of a unique bubble at (-5,70mm) for an SNR of -5 dB. The red cross indicates the true location of the bubble.

Figure 2 highlights lateral and axial profiles of the power maps in Figure 1, passing through the bubble. The averaged position of the maxima are regrouped in Table I. CMF-Elastic-net lateral lobe at -3dB is 0.1 mm, while it is 0.2 mm for RCB and 0.9mm for DAS. Its axial lobe is 1 mm, compared to 1.8 mm for RCB and 9.2 mm for DAS. It is also noticeable on this particular example that the maximum of RCB is shifted compared to the ground truth. The power map maximum averaged on 100 images is however close to the ground truth.

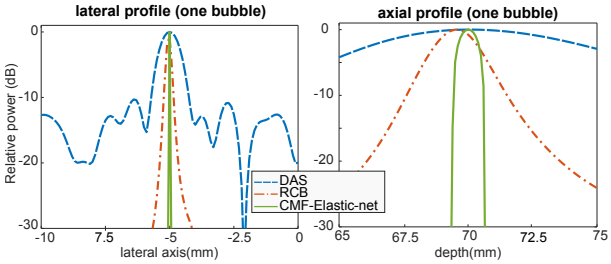

Fig. 2. Axial and lateral profiles of the power map for the one bubble configuration.

TABLE I
METRICS FOR ONE-BUBBLE CONFIGURATION

Metrics	Beamformer		
	DAS	***RCB***	***CMF-Elastic net***
Mean maximum position (mm) Truth: (-5,70)	(-5, 69.93)	(-5, 69.90)	(-5, 69.99)
Standard Deviation (mm)	0.35	0.28	0.34

C. Two bubbles laterally distributed

Figure 3 shows the power maps of two inertial sources with a lateral separation of 1.4 mm, for an SNR of 10dB.

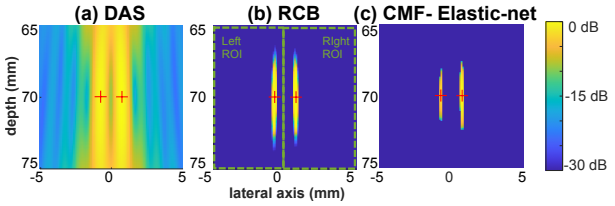

Fig. 3. Power maps of two bubbles laterally separated of 1.4 mm.

The lateral and axial profiles of the different maps are plotted on Figure 4. The lateral profile shows a good separation of the two bubbles for RCB and CMF-Elastic-net, while for DAS, there is a difference of 10 dB between the position of the bubbles and the pit between them. Table II regroups the quantitative metrics. For this configuration, the axial lobe is 3.4 mm for CMF-Elastic-net, 4.7 mm for RCB and 10 mm for DAS. Comparing the unique bubble configuration with the two bubbles one, one can see that the axial lobe of CMF-Elastic-net is larger (+2.4mm). The maxima are respectively calculated on different ROI (cf. Fig.3 .b).

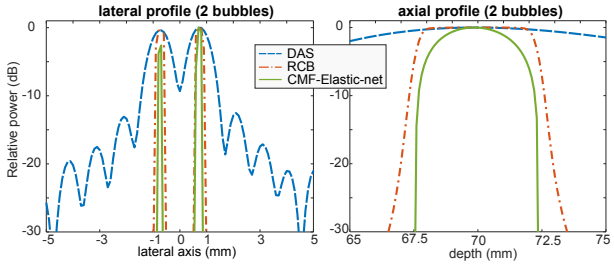

Fig. 4. Axial and lateral profiles for the configuration with 2 bubbles laterally spaced.

TABLE II
METRICS FOR TWO-BUBBLE LATERALLY DISTRIBUTED CONFIGURATION

Metrics	Beamformer		
	DAS	***RCB***	***CMF-Elastic net***
Mean maximum left ROI (mm) Truth: (-0.7,70)	(-0.7, 69.96)	(-0.7, 69.98)	(-0.7, 70.03)
Standard deviation left ROI (mm)	0.53	0.25	0.41
Mean maximum right ROI (mm) Truth: (0.7,70)	(0.7,70.06)	(0.7,70.04)	(0.7,70.11)
Standard deviation right ROI (mm)	0.55	0.26	0.43

D. Two bubbles axially distributed

Figure 5 shows the power maps of two inertial sources with an axial separation of 10 mm, at an SNR of 10dB.

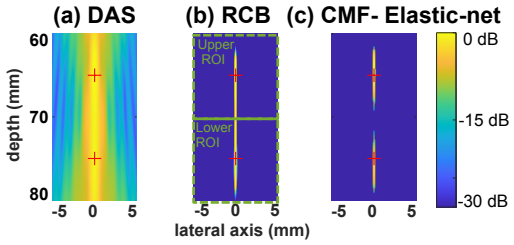

Fig. 5. Power maps of two bubbles 10 mm axially spaced.

Figure 6 shows the lateral and axial profiles of the sources extracted from the different maps. It can be observed from

the axial profile that there is no clear separation between the two bubbles with RCB and DAS. Conversely, it is possible to distinguish the two bubbles with CMF-Elastic-net, where the axial lobes at -3dB ar 4.7mm. However, as for the two laterally distributed sources, this axial profile shows a higher axial lobe for CMF-Elastic-net compared to the one bubble configuration (+3.7mm).

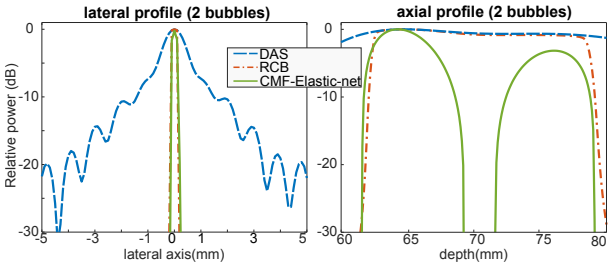

Fig. 6. Axial and lateral profiles of the configuration with 2 bubbles axially distributed.

TABLE III
METRICS FOR TWO-BUBBLE AXIALLY DISTRIBUTED CONFIGURATION

Metrics	Beamformer		
	DAS	***RCB***	***CMF-Elastic net***
Mean maximum upper ROI (mm) Truth: (0,65)	(0, 68.5)	(0, 66.86)	(0, 65.64)
Standard Deviation upper ROI (mm)	1.67	1.67	1.37
Mean maximum lower ROI (mm) Truth: (0,75)	(0, 71.28)	(0, 73.15)	(0, 74.18)
Standard Deviation lower ROI (mm)	1.83	1.45	1.78

IV. DISCUSSION AND CONCLUSION

This paper showed the interest of using inverse problems-based approaches for passive acoustic mapping of the inertial cavitation. Compared to the state-of-the-art, the proposed method improves the axial resolution and allows a better separation of sources in axially and laterally distributed sources. However, the axial lobes are more important when multiple sources are present than with one source. This effect could be due to partial coherence between the sources, that is not accounted for in this model. It is also important to notice that the choice of the penalization coefficients λ_1 and λ_2 is important. If λ_1 is too high, the algorithm tends to promote one source only. Conversely, if λ_2 is too high or λ_1 too small, the size of the lobes, primarily axial, would increase. Future work could focus on an automatic choice of penalization coefficients, accounting for coherence between sources, more complex regularization terms to penalize the presence of axial lobes and to combine multiple frequencies into the model.

ACKNOWLEDGMENT

This work was supported by the LABEX CELYA (ANR-10-LABX-0060) and LABEX PRIMES (ANR-11-LABX-0063) of Université de Lyon, within the program "Investissements d'Avenir" (ANR-11-IDEX-0007) operated by the French National Research Agency (ANR),as well as the "CAVIIAR" Project (ANR-22-CE19-0006), operated by the French National Research Agency (ANR).

REFERENCES

[1] D. L. Miller, N. B. Smith, M. R. Bailey, G. J. Czarnota, K. Hynynen, I. R. S. Makin, and B. C. of the American Institute of Ultrasound in Medicine, "Overview of therapeutic ultrasound applications and safety considerations," *Journal of ultrasound in medicine*, vol. 31, no. 4, pp. 623–634, 2012.

[2] M. Gyongy and C.-C. Coussios, "Passive spatial mapping of inertial cavitation during hifu exposure," *IEEE Transactions on Biomedical Engineering*, vol. 57, no. 1, pp. 48–56, 2009.

[3] P. Stoica, Z. Wang, and J. Li, "Robust capon beamforming," in *Conference Record of the Thirty-Sixth Asilomar Conference on Signals, Systems and Computers, 2002.*, vol. 1, pp. 876–880, IEEE, 2002.

[4] J. Li, P. Stoica, and Z. Wang, "On robust capon beamforming and diagonal loading," *IEEE transactions on signal processing*, vol. 51, no. 7, pp. 1702–1715, 2003.

[5] C. Coviello, R. Kozick, J. Choi, M. Gyöngy, C. Jensen, P. P. Smith, and C.-C. Coussios, "Passive acoustic mapping utilizing optimal beamforming in ultrasound therapy monitoring," *The Journal of the Acoustical Society of America*, vol. 137, no. 5, pp. 2573–2585, 2015.

[6] M. Polichetti, F. Varray, B. Gilles, J.-C. Béra, and B. Nicolas, "Use of the cross-spectral density matrix for enhanced passive ultrasound imaging of cavitation," *IEEE Transactions on Ultrasonics, Ferroelectrics, and Frequency Control*, vol. 68, no. 4, pp. 910–925, 2020.

[7] R. Merino-Martínez, P. Sijtsma, M. Snellen, T. Ahlefeldt, J. Antoni, C. J. Bahr, D. Blacodon, D. Ernst, A. Finez, S. Funke, *et al.*, "A review of acoustic imaging methods using phased microphone arrays: Part of the "aircraft noise generation and assessment" special issue," *CEAS Aeronautical Journal*, vol. 10, pp. 197–230, 2019.

[8] T. Yardibi, J. Li, P. Stoica, and L. N. Cattafesta III, "Sparsity constrained deconvolution approaches for acoustic source mapping," *The Journal of the Acoustical Society of America*, vol. 123, no. 5, pp. 2631–2642, 2008.

[9] H. Zou and T. Hastie, "Regularization and variable selection via the elastic net," *Journal of the Royal Statistical Society Series B: Statistical Methodology*, vol. 67, no. 2, pp. 301–320, 2005.

[10] A. Beck and M. Teboulle, "A fast iterative shrinkage-thresholding algorithm for linear inverse problems," *SIAM journal on imaging sciences*, vol. 2, no. 1, pp. 183–202, 2009.

[11] W. Lauterborn and T. Kurz, "Physics of bubble oscillations," *Reports on progress in physics*, vol. 73, no. 10, p. 106501, 2010.

[12] K. J. Haworth, K. B. Bader, K. T. Rich, C. K. Holland, and T. D. Mast, "Quantitative frequency-domain passive cavitation imaging," *IEEE transactions on ultrasonics, ferroelectrics, and frequency control*, vol. 64, no. 1, pp. 177–191, 2016.